The Astrophysical Journal Letters, 756:L13 (5pp), 2012 September 1 doi:10.1088/2041-8205/756/1/L13

A VIRIALIZED FILAMENTARY INFRARED DARK CLOUD

Audra K. Hernandez[1], Jonathan C. Tan[2], Jouni Kainulainen[3], Paola Caselli[4], Michael J. Butler[5], Izaskun Jiménez-Serra[6], and Francesco Fontani[7]
[1] Department of Astronomy, University of Wisconsin, Madison, WI 53706, USA; hernande@astro.wisc.edu
[2] Departments of Astronomy & Physics, University of Florida, Gainesville, FL 32611, USA
[3] Max-Planck-Institute for Astronomy, Königstuhl 17, D-69117 Heidelberg, Germany
[4] School of Physics & Astronomy, University of Leeds, Leeds LS2 9JT, UK
[5] Department of Astronomy, University of Florida, Gainesville, FL 32611, USA
[6] Harvard-Smithsonian Center for Astrophysics, 60 Garden Street, Cambridge, MA 02138, USA
[7] INAF-Osservatorio Astrofisico di Arcetri, Largo Enrico Fermi 5, I-50125 Firenze, Italy
Received 2012 June 27; accepted 2012 July 26; published 2012 August 10

ABSTRACT

The initial conditions of massive star and star cluster formation are expected to be cold, dense, and high column density regions of the interstellar medium, which can reveal themselves via near-, mid-, and even far-infrared absorption as infrared dark clouds (IRDCs). Elucidating the dynamical state of IRDCs thus constrains theoretical models of these complex processes. In particular, it is important to assess whether IRDCs have reached virial equilibrium, where the internal pressure balances that due to the self-gravitating weight of the cloud plus the pressure of the external environmental. We study this question for the filamentary IRDC G035.39–00.33 by deriving mass from combined NIR and MIR extinction maps and velocity dispersion from $C^{18}O$ (1–0) and (2–1) line emission. In contrast to our previous moderately super-virial results based on ^{13}CO emission and MIR-only extinction mapping, with improved mass measurements we now find that the filament is consistent with being in virial equilibrium, at least in its central parsec-wide region where $\sim$1000 $M_\odot$ snakes along several parsecs. This equilibrium state does not require large-scale net support or confinement by magnetic fields.

Key words: dust, extinction – ISM: clouds – stars: formation

Online-only material: color figures

1. INTRODUCTION

Identified by obscuration of the mid-infrared (MIR; i.e., $\sim$10 μm) Galactic background, infrared dark clouds (IRDCs) are likely to be representative of the initial conditions of massive star and star cluster formation, since their high mass surface densities ($\Sigma \gtrsim 0.1$ g cm^{-2}) and densities ($n_{\rm H} \gtrsim 10^4$ cm^3) are similar to regions with such star formation activity (e.g., Teyssier et al. 2002; Rathborne et al. 2006; Tan 2007; Butler & Tan 2009, hereafter BT09; Butler & Tan 2012, hereafter BT12; Zhang et al. 2009; Ragan et al. 2009).

The kinematics of IRDCs can be measured via their molecular line emission to determine if they are gravitationally bound and/or in virial equilibrium. Hernandez & Tan (2011, hereafter HT11) used ^{13}CO(1–0) emission from the Galactic Ring Survey (Jackson et al. 2006) to measure velocity dispersions in two filamentary IRDCs (F & H in the BT09 sample). Σ was estimated by averaging two methods: (1) MIR extinction (MIREX) mapping (BT09), given an assumed MIR opacity per gas mass and a foreground correction based on an analytic model of Galactic hot dust emission; (2) ^{13}CO emission, given an assumed abundance of this isotopologue. Cloud mass was then calculated assuming near kinematic distances to the IRDCs. A filamentary virial analysis following Fiege & Pudritz (2000, hereafter FP00) was performed in several orthogonal strips along the filaments. HT11 concluded surface pressure terms are dynamically important, suggesting that the filaments have not yet reached virial equilibrium.

Here we revisit this analysis for one of the filaments, G035.30–00.33 (H in the BT09/BT12 sample), which is 2.9 kpc distant with a few thousand solar masses of material spread over about 4 pc (projected) at its northern end. Although there are several 24 μm sources seen toward the filament (Carey et al. 2009), which are likely to be embedded protostars, most of the region appears MIR dark and starless. For our kinematic measurements, we use Insituto de Radioastronmía Millimétrica (IRAM) 30 m observations of $C^{18}O$ (1–0) and (2–1). The results of these and other molecular line observations are being presented in a series of papers on the formation and evolution of this filamentary IRDC. Paper I (Jiménez-Serra et al. 2010) presented maps of SiO, CO, ^{13}CO, and $C^{18}O$. Widespread SiO emission was observed, perhaps suggesting the presence of large-scale shocks that may have been involved in forming the filament. Paper II (Hernandez et al. 2011) compared the $C^{18}O$ and BT12 MIREX maps, showing CO suffers widespread gas-phase depletion in the IRDC by factors of up to $f'_D \simeq 5$, i.e., just one in five CO molecules remain in the gas phase. Paper III (this Letter) performs a filamentary virial analysis of the IRDC. Paper IV (Henshaw et al. 2012) studies the detailed kinematics of the filament and its surroundings, including analysis of the dense gas tracer N_2H^+.

2. MASS SURFACE DENSITY FROM EXTINCTION MAPPING

We use the MIREX Σ maps of BT12 combined with near-infrared (NIR; i.e., *J*, *H*, *K* (UKIRT Infrared Deep Sky Survey, Lawrence et al. 2007)) extinction maps (Kainulainen et al. 2011a) to yield a final map that has been presented by Kainulainen & Tan (2012, hereafter KT12). The MIREX map is derived from the 2″ resolution *Spitzer* IRAC 8 μm (Galactic Legacy Mid-Plane Survey Extraordinaire, GLIMPSE; Benjamin et al. 2003) image (Figures 1(a) and (b)). An MIR (band and background spectrum weighted) dust opacity per

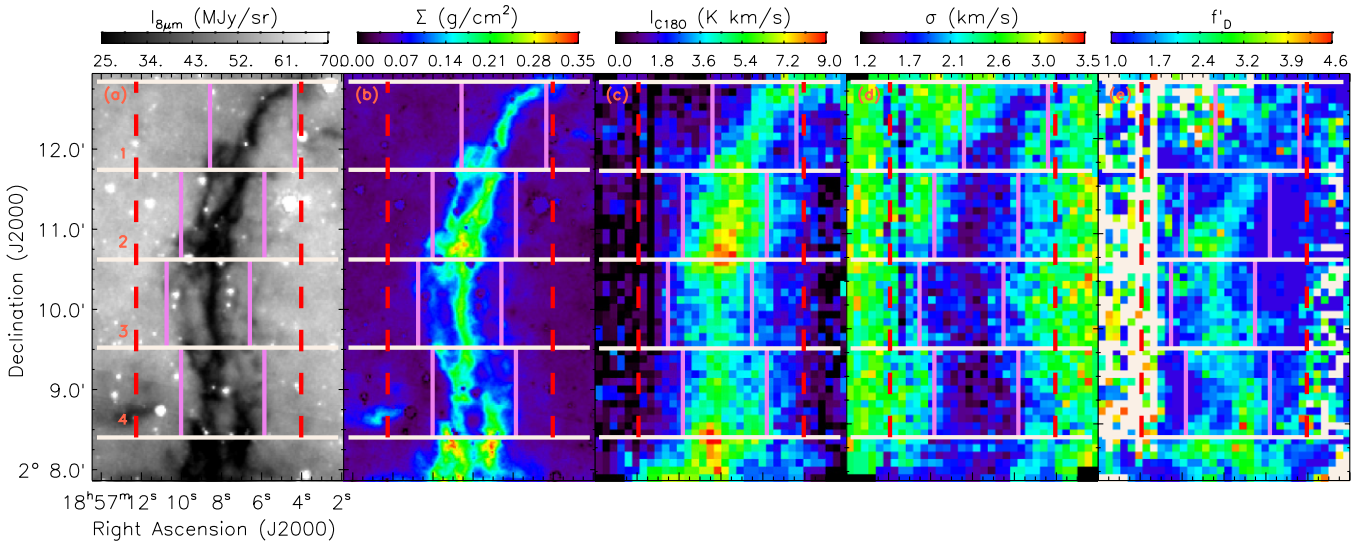

Figure 1. IRDC H (G035.30–00.33). (a) *Spitzer* GLIMPSE IRAC 8 μm image. Following HT11, four E–W strips (1–4 from N to S) have been drawn across the filament. Red dashed vertical lines delineate either side of the "Outer Filament." Magenta solid vertical lines define the "Inner Filament" regions, each half the width of the Outer Filament and centered on the center of mass of the strip. The image has 1.″2 pixels and point spread function with 2″ FWHM. (b) Total mass surface density, Σ, derived from (a) using the MIREX mapping method (BT12) with low mass surface density normalization set by NIR extinction mapping (KT12). (c) $C^{18}O$(2–1) emission integrated over velocities from 40–50 km s^{-1} (HT11), a pixel scale of 5″, and a beam size of 11″. (d) Total one-dimensional velocity dispersion, σ, derived from the $C^{18}O$(2–1) 40–50 km s^{-1} spectra. (e) Normalized CO depletion factor, f'_D, for regions with $\Sigma_{C18O} \geqslant 0.005$ g cm^{-2} (see the text).

(A color version of this figure is available in the online journal.)

unit total mass of $\kappa_{8\,\mu m} = 7.5$ cm^2 g^{-1} was adopted, consistent with the moderately coagulated thin ice mantle dust model of Ossenkopf & Henning (1994, hereafter OH94) and a gas-to-(refractory-component-)dust mass ratio of 156 (Draine & Lee 1984). We estimate that the uncertainties associated with these choices are ~30%, including those due to the grain composition and size distribution (e.g., the OH94 uncoagulated thin ice mantle model has opacities 0.83 times smaller; the maximally coagulated model 1.11 times larger; the bare grain, uncoagulated model 0.67 times smaller) and the gas-to-dust mass ratio (e.g., Draine 2011 estimates a ratio of 141 from depletion studies, 0.90 times smaller than our adopted value). Bright MIR sources lead to "holes" in the MIREX map. These cover just a small fraction of the projected area of the IRDC. They are excluded from the calculation of mean Σ.

The effect of BT12's use of an empirical foreground estimate (from observed saturation in independent cores) compared to BT09's analytic estimate is to increase Σ, especially in the densest regions, where it rises by up to a factor of ~3. The average increase of Σ inside the elliptical area of the IRDC defined by Simon et al. (2006) is a factor of 1.8.

In regions of low Σ near the edge of the cloud, the MIREX maps underestimate Σ since the technique is based on relative extinction of dense regions compared to the surroundings. This is now corrected for by combining the MIREX maps with NIR extinction maps (KT12). In regions where the NIR extinction map has $A_V < 10$ mag (~0.04 g cm^{-2}), it is used to set the zero point of the MIREX map. In higher column density regions, only the MIREX map is used, now with the zero point interpolated from the surroundings.

3. $C^{18}O$ OBSERVATIONS TO ESTIMATE VELOCITY DISPERSION AND CO DEPLETION

The $C^{18}O$ $J = 1$–0 and 2–1 transitions were mapped (on-the-fly) over a $2' \times 4'$ area with central position $\alpha(J2000) = 18^h57^m08^s$, $\delta(J2000) = 02°10'30''$ ($l = 35.°517$, $b = -0.°274$) using the IRAM 30 m telescope in Pico Veleta, Spain, in 2008 August and December with a combination of the ABCD (for $C^{18}O$(1–0)) and HERA ($C^{18}O$(2–1)) receivers (see Paper II for more details). At ~110 GHz ($J = 1 \rightarrow 0$), the beam size is 22″, while at ~220 GHz ($J = 2 \rightarrow 1$) it is 11″. Data were calibrated using GILDAS (CLIC). Spectra were regridded to a velocity resolution of 0.2 km s^{-1}.

The $C^{18}O$ emission from the IRDC is between velocities 40 and 50 km s^{-1} (HT11). The $C^{18}O$(2–1) integrated intensity map is shown in Figure 1(c). Standard analysis methods (correcting for excitation temperature and optical depth variations across the position–velocity cube) were used to derive the distribution of CO-emitting gas as a function of velocity (Paper II) and thus a map of total (thermal + nonthermal) one-dimensional velocity dispersion, σ, assuming mean particle mass $\mu = 2.33\,m_p$ (i.e., $n_{He} = 0.2 n_{H_2}$) and temperature of 15 K (Figure 1(d)). We assume σ is measured to about 10% accuracy. Note that the IRDC is clearly revealed as a region of relatively low σ. Mass surface density assuming a constant $C^{18}O$ abundance was derived via $\Sigma_{C18O} = 7.65 \times 10^{-2} (N_{C18O}/10^{16}\,\mathrm{cm}^{-2})$ g cm^{-2} (Paper II).

The ratio of mass surface density from NIR and MIR extinction, Σ (smoothed to the pixel scale of the CO data), and that from assuming a constant $C^{18}O$ abundance, Σ_{C18O}, defines the CO depletion factor $f_D \equiv \Sigma/\Sigma_{C18O}$ (averaged along a sight line through the cloud). To examine relative changes in depletion, following Paper II, we define a normalized depletion factor $f'_D = B f_D$, where B is a scaling factor so that f'_D is on average equal to 1 in regions with $0.01 < \Sigma/\mathrm{g\,cm}^{-2} < 0.03$. We find $B = 0.71$ compared to the Paper II value of 1.47 (Case 1 [i.e., no envelope subtraction] HiRes) due to changes in the Σ map, discussed above. For example, if CO is undepleted in this region and Σ correctly estimated, this would imply we underestimated the true $C^{18}O$ abundance by ~30%. The map of f'_D is shown in Figure 1(e), showing values for wherever $\Sigma_{C18O} \geqslant 0.005$ g cm^{-2}. Given the improved Σ map due to combination with NIR extinction data, this f'_D map supersedes

Table 1
IRDC Filament Properties

Cloud Property	Outer Filament (Strips 1–4, Total) ($R_f = 0.865$ pc, $R_e = 1.5R_f$)					Inner Filament (Strips 1–4, Total) ($R_f = 0.432$ pc, $R_e = 2.0R_f$)					% Error
	1_o	2_o	3_o	4_o	T_o	1_i	2_i	3_i	4_i	T_i	
$\bar{\Sigma}_{e,\rm off}$(E) (10^{-2} g cm^{-2})	3.09	2.79	3.13	4.54	3.39	4.44	4.13	3.82	3.55	3.98	30%
$\bar{\Sigma}_{e,\rm off}$(W) (10^{-2} g cm^{-2})	4.23	2.55	2.34	2.62	2.93	4.25	3.74	4.75	4.60	4.34	30%
$\bar{\Sigma}_f + \bar{\Sigma}_{e,\rm on}$ (10^{-2} g cm^{-2})	5.58	8.12	7.18	7.77	7.17	7.31	12.5	10.3	11.6	10.4	30%
$\bar{\Sigma}_e$ (10^{-2} g cm^{-2})	3.09	2.26	2.33	3.03	2.67	3.67	3.32	3.62	3.43	3.52	42%
$\bar{\Sigma}_f$ (10^{-2} g cm^{-2})	2.77	6.01	5.07	5.02	4.74	3.97	9.48	6.98	8.51	7.24	42%
M_e ($M_\odot$)	361	264	272	354	1250	287	259	283	268	1100	55%
M_f ($M_\odot$)	216	473	395	392	1480	155	370	272	332	1130	55%
$n_{{\rm H},e}$ (10^3 cm^{-3})	3.27	2.39	2.46	3.21	2.83	4.32	3.91	4.27	4.04	4.14	51%
$n_{{\rm H},f}$ (10^3 cm^{-3})	2.44	5.35	4.47	4.43	4.18	7.01	16.7	12.3	15.0	12.8	51%
m_f ($M_\odot$ pc^{-1})	199	435	363	360	340	142	340	250	305	259	51%
$\bar{v}_f$ (km s^{-1})	45.54	45.41	45.34	45.05	45.32	46.14	45.62	45.80	45.19	45.72	...
σ_f (km s^{-1})	1.59	1.47	1.37	1.25	1.36	1.17	1.31	1.01	1.01	1.08	10%
$m_{{\rm vir},f}$ ($M_\odot$ pc^{-1})	1180	1000	872	722	859	636	804	474	478	543	20%
$m_f/m_{{\rm vir},f}$	0.169	0.434	0.416	0.498	0.395	0.224	0.423	0.528	0.638	0.478	55%
P_f (10^{-12} cgs)	145	270	196	161	181	224	677	294	361	349	55%
$\bar{v}_e$ (km s^{-1})	45.51	44.79	44.97	44.70	45.06	45.58	44.99	44.83	44.77	45.03	...
σ_e (km s^{-1})	1.63	1.60	1.52	1.68	1.53	1.50	1.40	1.25	1.28	1.34	10%
P_e (10^{-12} cgs)	204	143	134	211	154	229	180	156	155	174	55%
P_e/P_f	1.41	0.528	0.681	1.31	0.853	1.02	0.265	0.532	0.430	0.499	41%
$t_{s,f} = 2R_f/\sigma_f$ (Myr)	1.06	1.15	1.23	1.35	1.24	0.723	0.646	0.837	0.837	0.783	20%
$t_{D,f} = 0.16 n_{{\rm H},f,4}^{-1}$ (Myr)	0.66	0.30	0.36	0.36	0.38	0.23	0.096	0.13	0.11	0.13	>51%
f_D	3.35	2.23	2.68	3.24	2.88	2.68	2.36	2.57	2.65	2.57	50%
f'_D	2.37	1.57	1.89	2.29	2.04	1.89	1.67	1.81	1.88	1.81	50%

that of Paper II: in particular, it extends to regions of lower mass surface density. However, the basic structure is unchanged, with maximum values of $f'_D \simeq 5$ in the highest column density cores.

4. FILAMENTARY VIRIAL ANALYSIS

4.1. Filament and Envelope Geometry

We assume the filament is locally cylindrical, with radius R_f, and symmetrically embedded in a cylindrical envelope of outer radius R_e (and inner radius $R_{f\_}$). To derive the mean mass surface density of the filament $\bar{\Sigma}_f$, we need to subtract the contribution from the overlapping portion of the envelope, $\bar{\Sigma}_{e,\rm on}$. For a uniform density envelope and for negligible net contribution of material outside R_e, we first measure $\bar{\Sigma}_{e,\rm off}$, i.e., of the observed envelope region that is offset in projection from the filament, by averaging the two parts of each strip that are at projected distances between R_f and R_e from the filament's central axis. From simple geometry, the mean mass surface density of the whole envelope, $\bar{\Sigma}_e$, is related to $\bar{\Sigma}_{e,\rm off}$ via

$$\bar{\Sigma}_e = \frac{\pi \sin^2\theta(1-\cos\theta)}{2\theta - \sin 2\theta}\bar{\Sigma}_{e,\rm off}, \quad (1)$$

where $\cos\theta = R_f/R_e$. Thus, since $\bar{\Sigma}_e = (R_f/R_e)\bar{\Sigma}_{e,\rm on} + ([R_e - R_f]/R_e)\bar{\Sigma}_{e,\rm off}$, we have

$$\bar{\Sigma}_{e,\rm on} = \frac{R_e}{R_f}\bar{\Sigma}_e - \frac{R_e - R_f}{R_f}\bar{\Sigma}_{e,\rm off}. \quad (2)$$

As shown in Figure 1, we consider two cases: (1) an "Outer Filament" (red lines in Figure 1) of diameter 2.′05 in R.A. and for which $R_e = 1.5R_f$ (set by the extent of the C^{18}O observations), i.e., $\theta = 0.841$ radians, $\bar{\Sigma}_e = 0.845\bar{\Sigma}_{e,\rm off}$ and $\bar{\Sigma}_{e,\rm on} = 0.768\bar{\Sigma}_{e,\rm off}$. Each of the four strips is centered at $\alpha(J2000) = 18^{\rm h}57^{\rm m}08\overset{\rm s}{.}02$ and is 1.′12 wide in decl., with the strip 2–3 boundary at $\delta(J2000) = 02^\circ 10' 35\overset{''}{.}7$. This was the same size and location of the filament region adopted by HT11. (2) An "Inner Filament" (magenta lines in Figure 1) that we set to have half the Outer Filament width and to have $R_e = 2.0\,R_f$, i.e., $\theta = 1.047$, $\bar{\Sigma}_e = 0.959\bar{\Sigma}_{e,\rm off}$, and $\bar{\Sigma}_{e,\rm on} = 0.918\bar{\Sigma}_{e,\rm off}$. Now within each strip, the location of the Inner Filament is centered on the center of mass of the whole strip, so this case follows the structure of the filament more accurately. The correction factors for the above two cases were applied to estimate $\bar{\Sigma}_e$ and $\bar{\Sigma}_f$. This division of the cloud into filament and envelope regions is quite idealized, but is necessary for comparison with analytic models.

The velocity dispersion of the envelope, σ_e, is measured from the average spectra of the E and W envelope "off" regions in each strip. Then the above factors for estimating contributions from an overlapping envelope are also applied to the C^{18}O spectra: the spectrum of the filament is derived from the observed "on" spectrum minus the envelope "off" spectrum scaled by 0.768 and 0.918 for Outer and Inner cases, respectively. This subtracted spectrum is used to derive the total one-dimensional velocity dispersions in the filament, σ_f. For both σ_e and σ_f, only those parts of the spectra with signal $\geqslant$1 standard deviation of the noise level are used.

For each strip and for both Outer and Inner cases, the properties of the filament and envelope are listed in Table 1. In addition to the 30% error we assume for the estimates of the directly observed values of Σ (see Section 2), we also include an additional 30% error (added in quadrature) for parameters that depend on the assumed cylindrical filament geometry, i.e., $\bar{\Sigma}_e$

and $\bar{\Sigma}_f$. Without direct observational constraints, we further assume the filament axis is inclined by $i = 60^\circ \pm 15^\circ$ to our line of sight (90° would be in the plane of the sky). This uncertainty contributes up to 22% uncertainty to quantities such as the mass per unit length of the filament. The distance to the filament is assumed to be 2.9 ± 0.5 kpc (Simon et al. 2006). This uncertainty is equivalent to non-circular motions of $\sim 8\,\mathrm{km\,s^{-1}}$.

4.2. Comparison to Fiege–Pudritz Models of Virial Equilibrium

We perform a filamentary virial analysis following FP00, who showed pressure-confined, non-rotating, self-gravitating, filamentary (i.e., lengths ≫ widths) magnetized clouds that are in virial equilibrium satisfy

$$\frac{P_e}{P_f} = 1 - \frac{m_f}{m_{\mathrm{vir},f}}\left(1 - \frac{\mathcal{M}_f}{|W_f|}\right). \quad (3)$$

Here, $P_e = \rho_e \sigma_e^2$ (with $\rho_e = \mu_{\mathrm{H}} n_{\mathrm{H},e}$, with mass per H nucleus of $\mu_{\mathrm{H}} = 1.4\, m_p = 2.34 \times 10^{-24}$ g) is the external pressure at the surface of the filament assumed to be equal to the mean envelope pressure, $P_f = \rho_f \sigma_f^2$ is the mean total pressure in the filament, m_f is the mass per unit length of the filament, $m_{\mathrm{vir},f} \equiv 2\sigma_f^2/G$ is its virial mass per unit length, $\mathcal{M}_f$ is its magnetic energy per unit length (associated with large-scale static magnetic fields providing either support or confinement), and $W_f = -m_f^2 G$ is its gravitational energy per unit length.

We can measure P_e/P_f and $m_f/m_{\mathrm{vir},f}$ for the Outer and Inner Filament cases for each strip (Table 1). No information is currently available for $\mathcal{M}_f$. In Figure 2, we thus compare the observed filament properties to a series of models that vary the contribution of magnetic support ($\mathcal{M}_f/|W_f| > 0$ from poloidally dominated B-fields) or confinement ($\mathcal{M}_f/|W_f| < 0$ from toroidally dominated B-fields).

Figure 2 indicates that as one zooms from the Outer to Inner Filaments, P_e/P_f decreases and $m_f/m_{\mathrm{vir},f}$ tends to increase. Within the uncertainties, the Inner Filament (and much of the Outer) is consistent with the model of virial equilibrium not requiring any magnetic support or confinement ($\mathcal{M}_f/|W_f| = 0$). Stated another way, for the Inner Filament the internal pressures are factors of a few greater than external. Such pressure enhancements are consistent with those expected from self-gravity given the observed masses and velocity dispersions. Note that the relative positions of the strips in Figure 2 are more accurately known than the error in any one position, since systematic uncertainties are shared. These relative positions, especially that of strip 4 with respect to 2 and 3, further support the hypothesis that much of the filament is in virial equilibrium with a common, small degree of support from large-scale B-fields.

We have tested the sensitivity of our results to our adopted method of envelope subtraction: if no correction to filament properties due to the presence of an overlapping envelope is allowed for, then for the Inner Filament we derive σ_f to be 12% lower, P_e/P_f to be 23% lower, and $m_f/m_{\mathrm{vir},f}$ to be 30% higher. These values are still consistent with virial equilibrium without needing large-scale magnetic support or confinement.

Our results are different from those of HT11, who concluded that, for the Outer Filament, the surface pressures were all greater than the internal ones. For Outer Filament strips 1–4, they found $P_e/P_f = 3.06, 1.74, 3.32, 5.25$. Our values are factors of 0.46, 0.30, 0.21, 0.25 smaller, respectively. For these strips HT11 found $m_f/m_{\mathrm{vir},f} = 0.0789, 0.161, 0.269, 0.367$. Our values are factors of 2.1, 2.7, 1.5, 1.4 larger, respectively. These differences are mostly due to our use of improved Σ estimation methods. The BT12 MIREX map improves the estimate of MIR foreground intensity, which increases the derived values of Σ in the denser parts of the filament. Furthermore, we now no longer use CO line intensities to derive Σ: HT11 used ^{13}CO line intensities as one method and then averaged with the BT09 MIREX value. The ^{13}CO-derived values were generally lower than the BT09 MIREX values, which we now attribute as due to CO depletion (Paper II). Thus, our estimates of Σ and mass have now increased by factors of a few compared to HT11, causing P_e/P_f to decrease and $m_f/m_{\mathrm{vir},f}$ to increase. Our present study uses C^{18}O to measure velocity dispersions, which is less prone to being affected by optical depth effects than the ^{13}CO used by HT11 (although HT11 did correct for optical depth). For the Outer Filament strips 1–4, HT11 found $\sigma_f = 1.52, 1.34, 1.03, 0.995\,\mathrm{km\,s^{-1}}$. Our C^{18}O-derived values are factors 1.05, 1.10, 1.33, 1.26 times larger. The higher angular resolution of the C^{18}O(2–1) observations allow us to probe to smaller scales, i.e., the narrower Inner Filament case, where line widths are seen to decrease by factors of about 0.8 compared to the Outer Filament (Figure 1(d)). Therefore, the overall velocity dispersions adopted here for the filament are quite similar to those of HT11 and the differences in our results are thus rather caused by the higher Σ's now derived.

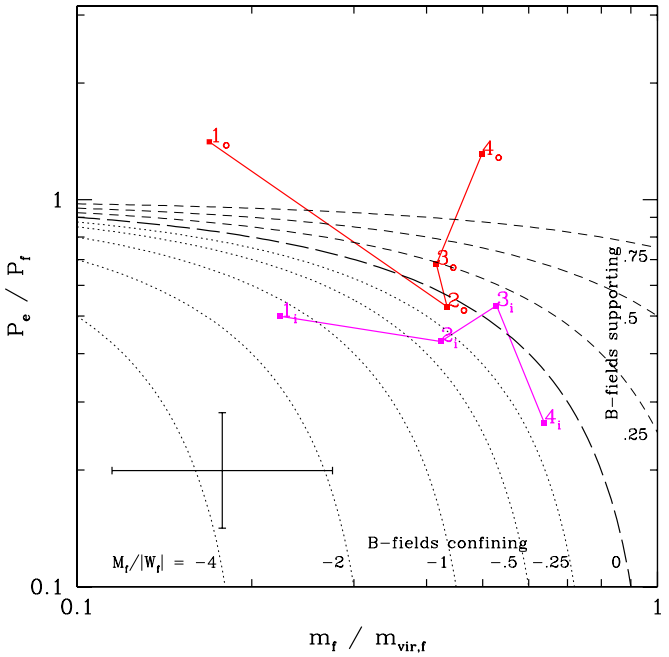

Figure 2. Ratio of surface to internal pressure, P_e/P_f, vs. ratio of mass per unit length to virial mass per unit length, $m_f/m_{\mathrm{vir},f}$, for strips 1–4 of IRDC H. Red line and points labeled $\#_o$ show the "Outer Filament." Magenta line and points labeled $\#_i$ show the "Inner Filament." The error bars in the lower left show typical uncertainties. The smooth curves show the conditions satisfied by Equation (3) for confining magnetic fields with $\mathcal{M}_f/|W_f| < 0$ (dotted lines), supporting magnetic fields with $\mathcal{M}_f/|W_f| > 0$ (dashed lines), and no magnetic fields, i.e., $\mathcal{M}_f/|W_f| = 0$ (long-dashed line). The results for the Inner Filament indicate a dynamical state consistent with magnetically neutral virial equilibrium.

(A color version of this figure is available in the online journal.)

5. DISCUSSION

There is some evidence that the IRDC H filament may have formed recently from converging flows of molecular gas.

Jiménez-Serra et al. (2010, Paper I) reported widespread, more than parsec-scale SiO emission from the filament, which may have resulted from large-scale shocks with speeds of at least several km^{-1}. Henshaw et al. (2012, Paper IV) studied the kinematics of the region and found evidence for the formation of the main filament via the merging flow of surrounding filaments observed in C^{18}O (with typical densities of $n_{\rm H,flow} \sim 10^3$ cm^{-3}). They find that the line of sight relative velocity between each component of the merging flow and the main filament is $v_{\rm flow} \sim 3$ km s^{-1}.

If the main filament has formed relatively recently, is this consistent with its observed state of near virial equilibrium? It should take at least a signal crossing time, $t_{s,f} = 2R_f/\sigma_f$, for a region of the filament to settle into virial equilibrium. These times are ~0.8 Myr for the Inner Filament (Table 1). To form the filament from two converging flows takes a time $t_{{\rm form},f} = 0.236(m_f/100\,M_\odot\ {\rm pc}^{-1})/[(R_f/{\rm pc})(v_{\rm flow}/3\ {\rm km\ s}^{-1})(n_{\rm H,flow}/10^3\,{\rm cm}^{-3})]$ Myr. Applying this to the average properties of the Inner Filament ($R_f = 0.432$ pc, $m_f = 259\,M_\odot$), yields $t_{{\rm form},f} = 1.4$ Myr (see also Paper IV). Thus, even in the scenario of a recently formed filament, enough time should have elapsed for it to have settled into virial equilibrium.

The widespread CO depletion observed in Paper II and here (Figure 1(e)) also constrains the age of the filament. The CO depletion time is $t_{D,f} = 0.16(n_{{\rm H},f}/10^4\,{\rm cm}^{-3})^{-1}$ Myr, assuming a sticking probability of order unity (Tielens & Allamandola 1987). Table 1 lists $t_{D,f}$ for the different strips. For the Inner Filament, these are relatively short, ~0.1 Myr, which thus provides a lower limit for its age.

The implications of virial equilibrium of self-gravitating IRDC filaments are profound. If this result for G035.39–00.33 applies more generally to IRDCs, then it indicates that the *initial conditions* for star formation, including the cores that form massive stars and the clumps that form star clusters, are created from environments where approximate pressure equilibrium has been established. The value of this pressure is set by the self-gravitating weight of the larger scale cloud, i.e., the IRDC, which dominates over the pressure of its surrounding environment (unlike for most clumps in giant molecular clouds: e.g., Bertoldi & McKee 1992; Kainulainen et al. 2011b). This would confirm a basic assumption of the initial conditions of the core accretion model of massive star formation of McKee & Tan (2002, 2003) and is also expected under the scenario of equilibrium star cluster formation (Tan et al. 2006). The fact that our results differ from those of HT11 highlights the importance of improved estimates of masses and surface pressures of IRDCs. These effects may help explain other reported discrepancies between dynamical (i.e., virial) masses and true masses (e.g., Battersby et al. 2010). Measurement of large-scale magnetic field strengths and geometries in IRDCs would help to further constrain the models.

We thank Bruce Draine and an anonymous referee for helpful comments and discussions that improved the Letter. J.C.T. acknowledges support from NSF CAREER grant AST-0645412, NASA Astrophysics Theory and Fundamental Physics grant ATP09-0094, and NASA Astrophysics Data Analysis Program ADAP10-0110. A.K.H. acknowledges support from *HST* grants HST-GO-112275 and HST-GO-12276 to Bart Wakker at the University of Wisconsin. Finally, we would like to acknowledge the IRAM facilities and staff.

REFERENCES

Battersby, C., Bally, J., Jackson, J. M., et al. 2010, ApJ, 721, 222
Benjamin, R. A., Churchwell, E., Babler, B. L., et al. 2003, PASP, 115, 953
Bertoldi, F., & McKee, C. F. 1992, ApJ, 395, 140
Butler, M. J., & Tan, J. C. 2009, ApJ, 696, 484 (BT09)
Butler, M. J., & Tan, J. C. 2012, ApJ, 754, 5 (BT12)
Carey, S. J., Noriega-Crespo, A., Mizuno, D. R., et al. 2009, PASP, 121, 76
Draine, B. T. 2011, Physics of the Interstellar and Intergalactic Medium (Princeton, NJ: Princeton Univ. Press)
Draine, B. T., & Lee, H. M. 1984, ApJ, 285, 89
Fiege, J. D., & Pudritz, R. E. 2000, MNRAS, 311, 85 (FP00)
Henshaw, J. D., Caselli, P., Fontani, F., et al. 2012, MNRAS, submitted (Paper IV)
Hernandez, A. K., & Tan, J. C. 2011, ApJ, 730, 44 (HT11)
Hernandez, A. K., Tan, J. C., Caselli, P., et al. 2011, ApJ, 738, 11 (Paper II)
Jackson, J. M., Rathborne, J. M., Shah, R. Y., et al. 2006, ApJS, 163, 145
Jiménez-Serra, I., Caselli, P., Tan, J. C., et al. 2010, MNRAS, 406, 187 (Paper I)
Kainulainen, J., Alves, J., Beuther, H., Henning, T., & Schuller, F. 2011a, A&A, 536, 48
Kainulainen, J., Beuther, H., Banerjee, R., Federrath, C., & Henning, T. 2011b, A&A, 530, 64
Kainulainen, J., & Tan, J. C. 2012, ApJ, submitted (KT12)
Lawrence, A., Warren, S. J., Almaini, O., et al. 2007, MNRAS, 379, 1599
McKee, C. F., & Tan, J. C. 2002, Nature, 416, 59
McKee, C. F., & Tan, J. C. 2003, ApJ, 585, 850
Ossenkopf, V., & Henning, T. 1994, A&A, 291, 943 (OH94)
Ragan, S. E., Bergin, E. A., & Gutermuth, R. A. 2009, ApJ, 698, 324
Rathborne, J. M., Jackson, J. M., & Simon, R. 2006, ApJ, 641, 389
Simon, R., Rathborne, J. M., Shah, R. Y., Jackson, J. M., & Chambers, E. T. 2006, ApJ, 653, 1325
Tan, J. C. 2007, in IAU Symp. 237, Triggered Star Formation in a Turbulent ISM, ed. B. G. Elmegreen & J. Palous (Cambridge: Cambridge Univ. Press), 258
Tan, J. C., Krumholz, M. R., & McKee, C. F. 2006, ApJ, 641, L121
Teyssier, D., Hennebelle, P., & Perault, M. 2002, A&A, 382, 624
Tielens, A. G. G. M., & Allamandola, L. J. 1987, in NATO ASIC Proc. 210: Physical processes in Interstellar Clouds, ed. G. E. Morfill & M. Scholer (NATO Sci. Ser. C; New York: Springer), 333
Zhang, Q., Wang, Y., Pillai, T., & Rathborne, J. 2009, ApJ, 696, 268